remote sensing

Article

Lake Turbidity Mapping Using an OWTs-bp Based Framework and Sentinel-2 Imagery

Sijia Li [1,2], Tiit Kutser [3], Kaishan Song [1,*], Ge Liu [1] and Yong Li [1]

1 Key Laboratory of Wetland Ecology and Environment, Northeast Institute of Geography and Agroecology, Chinese Academy of Sciences, Changchun 130102, China
2 Key Laboratory of Space Ocean Remote Sensing and Application, Ministry of Natural Resources, National Satellite Ocean Application Service, Beijing 100081, China
3 Estonian Marine Institute, University of Tartu, 12618 Tallinn, Estonia
* Correspondence: songks@iga.ac.cn; Tel.: +86-0431-85542364

Abstract: Lake turbidity, representing a general indicator of water 'cloudiness', is a key parameter in many monitoring programs. It is not possible to cover all lakes with frequent in situ monitoring. Sentinel-2 MultiSpectral Imager (MSI) can help to fill the gaps if a robust turbidity retrieval methodology is developed. Previously published results demonstrated the usefulness of MSI at a limited regional scale, while our aim was to develop methodology that allows monitoring turbidity over the whole of China. We proposed methodology with a reflectance that can be classified into optical water types (OWTs), and then a back propagation neural network model (BP-TURB) is used to estimate turbidity. The reflectance of in situ lake samples extracted from MSI imagery was clustered as three OWTs, and validation performance was satisfactory: $R^2 > 0.81$, RMSE < 17.54, and MAE < 11.20. This allowed us to map turbidity in all Chinese lakes, of which the area is larger than 1 km^2. A larger percentage of clear lakes (53.26%) with low turbidity levels (<10 NTU) was found in 2020 than in 2015 (37.43%). Lakes in the plateau regions generally exhibited lower turbidity than those situated in the plains regions, for which the turbidity patterns were determined by lake volume, averaged depth, and elevation. We demonstrated that the Sentinel-2 MSI data with the novel approach proposed by us allows for mapping lake turbidity over a large variety of lakes and extensive geographic conditions, as well as for revealing temporal changes in these lakes and their links to lake abiotic characteristics.

Keywords: turbidity; Chinese lakes; Sentinel-2; MSI; abiotic factors

check for updates

Citation: Li, S.; Kutser, T.; Song, K.; Liu, G.; Li, Y. Lake Turbidity Mapping Using an OWTs-bp Based Framework and Sentinel-2 Imagery. *Remote Sens.* **2023**, *15*, 2489. https://doi.org/10.3390/rs15102489

Academic Editors: Frédéric Frappart, Luc Bourrel, Thibault Catry and Pham-Duc Binh

Received: 2 March 2023
Revised: 13 April 2023
Accepted: 28 April 2023
Published: 9 May 2023

Copyright: © 2023 by the authors. Licensee MDPI, Basel, Switzerland. This article is an open access article distributed under the terms and conditions of the Creative Commons Attribution (CC BY) license (https://creativecommons.org/licenses/by/4.0/).

1. Introduction

Lakes play a major role in ecology, industry, agriculture, and human wellbeing by receiving runoff and regulating climate, providing drinking and irrigation water, and supporting recreation, among other services and functions [1,2]. Turbidity, representing the "cloudiness" of lakes [3], is seen as a general indicator of scattering capabilities, jointly modulated by the presence of all optically active substances [4,5]. Turbidity was defined as the 90° side-scattering of light (at 860 nm) in relation to Formazin, a chemical standard that is sensitive to particle composition [6] under high-intensity scattered light. Hence, turbidity is often reported in nephelometric turbidity units (NTU), and is associated with lakes' biogeochemical metabolism, e.g., nutrient or pollutant dynamics and sediment transport by geomorphologic and hydrological processes. Higher turbidity reduces the depth of penetration of light, meaning that light is absorbed in a thinner layer [7]. Consequently, radiative heating and lake stratification depend on turbidity and the changes in it [7,8]. Long-term trends and short-term dynamics of lake turbidity provide the knowledge on environmental health and changes in the catchment. Given these beneficial functions and importance, monitoring the turbidity of lakes is useful to protecting and managing the ecological functions of aquatic ecosystems [9].

Satellite data have been used in mapping water turbidity since Moore (1980) [10] assessed the feasibility of satellite data. The remote sensing of turbidity has been employed as an early alert for changes in lake ecosystems [11,12]. The advantage of remote sensing is the ability to survey large spatial extent and hard to access areas [13]. Many satellites launched in the past decades also provide technical capabilities to map lake turbidity; for example, the European Space Agency has launched several sensors, e.g., Medium Resolution Imaging Spectrometer, MERIS, on Envisat; Ocean and Land Colour Instrument, OLCI, on Sentinel-3A and B; and MultiSpectral Instrument, MSI, on Sentinel-2A and B. The National Aeronautics and Space Administration (NASA) launched Landsat series satellites [14], and they are suitable for turbidity mapping. However, there are no satellite sensors that were specifically designed for inland waters, i.e., that have good spatial resolution necessary for smaller waters and sufficient sensitivity and spectral bands needed for water quality monitoring. However, the MSI sensor captured the interest of the research community [15–18]. It has a high spatial resolution (10 m $\times$ 10 m at nadir), is acceptable for water quality remote sensing spectral resolution in the visible and near infrared ranges, has sufficient sensitivity for most lakes, and has relatively high temporal resolution (every 2–5 days with two satellites). There are commercial satellite systems with very high spatial resolution. However, the cost of using such imagery over large areas and with high temporal frequency is prohibitive, whereas Sentinel-2 imagery is free of charge. Turbidity monitoring requires rapid sensing due to the dynamic environment, with a continuous supply of nutrients, particles, and organic matter via runoff or rainfall, and sediment resuspension. Consequently, the use of MSI is a reasonable compromise for a low-cost, high spatial resolution, and frequent revisit time (every 2–3 days at mid-latitudes) monitoring of lake water quality over large areas.

The Copernicus Land Monitoring Service (CLMS) also has a turbidity product that is based on Sentinel-2 data, but it is provided at 100 m spatial resolution, meaning that it is not sufficient for smaller lakes. For example, 32,843 lakes are located in Tibet, and around 96% of them are small and in China [19]. Moreover, this product is provided only for Europe and Africa, not for Asia. Additionally, previous studies of Chinese lakes provided strictly lake "regional" products [11,20,21]. Nationwide turbidity monitoring cannot be performed based on these regional algorithms. On the other hand, the turbidity parameter of the Copernicus program is derived from the suspended particulate matter, with algorithms depending on the optical water types. This is due to the strong relationship between turbidity and total suspended solids; a low-cost turbidity measurement can be used to estimate total suspended solids instead of a traditional gravimetric method in a lab [20,22]. However, this process could bring more uncertainties because the turbidity was a comprehensive index incorporating the optically active water constituents [23]. They also contribute reflectance signals and are even higher in lakes where phytoplankton particles dominate the optical properties or algal blooms are frequent. However, several sources of uncertainty for portable SPM (suspended particulate matter) algorithms are expected to influence the magnitude in uncertainties from reflectance signals. When this comparison with in situ measurement was applied to a dataset as a whole, it showed uncertainties from reflectance signals in pixels that were subsequently propagated to any derived turbidity products on specific algorithm sensitivities [24]. Additional effort strongly demonstrated that it will be needed to properly develop the turbidity algorithm responding to MSI sensor.

Several existing algorithms have been suggested for deriving turbidity from the red part of the reflectance spectrum for low-to-moderate turbidity values. These approaches generally can be grouped into semi-analytical [25], empirical (for recent reviews see, e.g., Lien Rodríguez-López et al., 2021; Maltese et al., 2013) [26,27], reflectance band combinations, and machine learning algorithms [11]. It is widely known that empirical band ratio algorithms are site-specific and cannot be applied over a large variety of lakes [28]. There are several ways to avoid the shortcomings of empirical methods. For example, analytical (physics based) methods can be used. However, these methods are sensitive to atmospheric correction errors, and atmospheric correction is still an unsolved problem in inland water remote sensing. Another approach, also used by the CLMS, is dividing lakes according to optical water types (OWTs) and then using a specific set of algorithms for each OWT [29,30]. It would be desirable to derive an accurate estimate by per-pixel similarities of reflectance to a set of OWTs. Likewise, a universal turbidity algorithm without the requirements of region-specific adaptation or calibration could be appreciated for the fast-growing automated processing of satellite imagery. It could be expected that some distinct, but complementary, methodologies for retrieving turbidity could respond to lake-specific difference issues in a large-scale observation. Therefore, our focus was on the turbidity characterization scheme of the final turbidity product in relation to OWTs. To address this need, the aim of this study was to develop a methodology that allowed for monitoring turbidity in all lakes in China that are larger than 1 km^2 in size. We chose the OWT-guided neural network approach to achieve this. More importantly, we achieved Chinese turbidity maps and discussed the main forcing factors.

2. Study Region

China covers a total of 9.6 million square kilometers. Its geomorphology is extremely complex, and there are three terrain steps from the Qinghai-Tibetan Plateau (averaged elevations >4000 m, dominated by grassland), to the Kunlun Mountains (elevation ranges 1000–2000 m), and the eastern hills and plains (mostly below 500 m from the average sea level). The latter region can be characterized through intensive agricultural and other anthropogenic activities (Figure 1). There were 2554 (in 2015) and 2693 (in 2020) natural lakes (surface area >1 km^2) distributed across China, respectively (National Tibetan Plateau Data Centre) [19] (Figure S1).

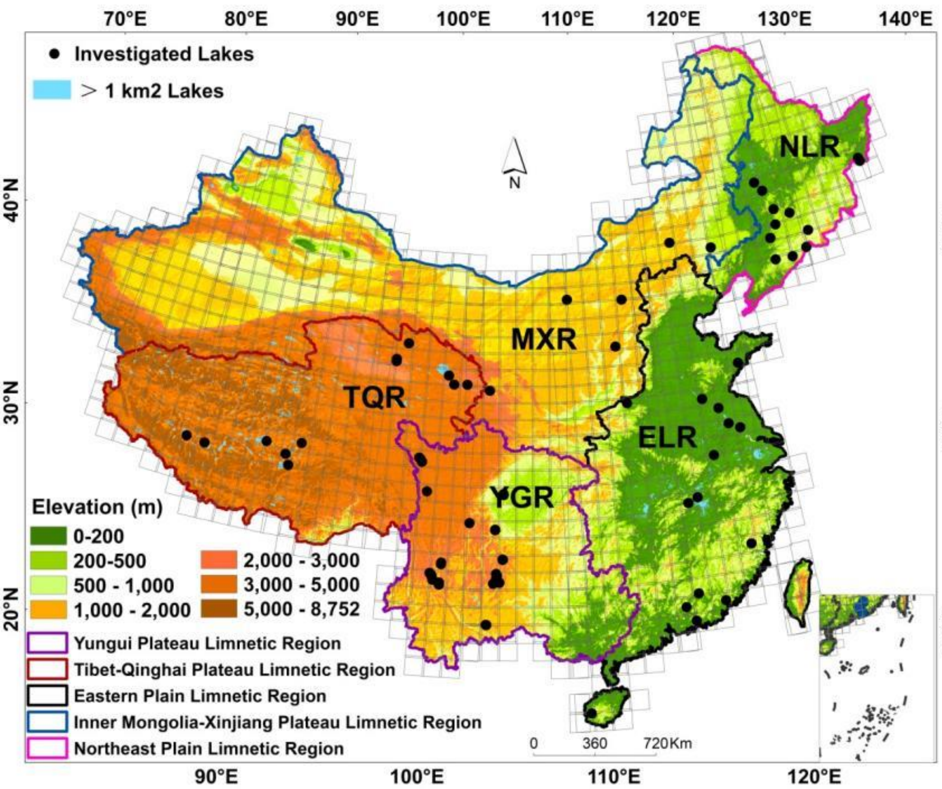

Figure 1. Location of lakes where in situ measurements of trophic parameters, e.g., Chl–a, SDD, and TP, were made. See text for a description of each data source.

3. Methods

3.1. In Situ Water Quality Collection and Field Measurements

In 2017–2019, a total of 484 samples from 66 lakes were collected during the highly productive season (April to October) (Figure 1 and Table S1). Results of some of these measurements were published in our previous studies [16,31–33]. We used five lake zones as defined by Wang and Dou (1998, Early National Investigation) [34] (Supplementary Materials). These lakes spanned over a range of sizes, elevations, water qualities, and environments (e.g., climatic zones), suggesting large-scale bio-optical variability (Figure S1, Gross Domestic Product, population, land-use, digital elevation model, temperature, and precipitation, etc.). More detailed descriptions of the five lake regions can be found in the Supplementary Materials.

3.2. Water Quality and Light Absorption Determination in Laboratory

The turbidity values (Turb), Chlorophyll-a (Chl–a), suspended matter (SPM), and total nitrogen (TN) and total phosphorus (TP) concentrations (APHA/AWWA/WEF, 1998) [35] were determined in the laboratory. Note that we only measured suspended matter and turbidity for some representative lakes in the YGR (Lakes 48–66, Lakes 31–22, Table S1). The absorption coefficients of optically active substances, e.g., CDOM [$a_{\mathrm{CDOM}}(\lambda)$], total particulate matter [$a(\lambda)$], and non-algal particles [$a_{\mathrm{d}}(\lambda)$], were determined by the quantitative filtration technique [36]. More details can be found in the Supplementary Materials. We used absorption values at 443 nm to characterize the amount of CDOM, $a_{\mathrm{CDOM}}(443)$.

3.3. MSI Imagery Match-Ups

Sentinel-2A/B MSI Level 1C data can be freely acquired from the Copernicus Open Access Hub of the European Space Agency (ESA, https://scihub.copernicus.eu/, accessed on 16 October, 2021). The Level-1C products were calibrated radiometrically for viewing geometry and orthorectified into a WGS84 projection. All the Sentinel-2 MSI images were atmospherically corrected using the C2RCC processor, producing normalized water reflectance *rhown*(λ) at 443, 492, 560, 665, 704, and 740 nm. This is also consistent with the atmospheric correction validation in earlier studies [17,37]. We used a 3 × 3 pixel centered reflectance to create match-ups with in situ data. Only images with no cloud contamination (<10%) were used for analysis. Altogether, 198 Sentinel-2 scenes were found that were within a ±7 days' time window and were used in the match-up analyses. Toming et al. (2016) [15] confirmed that the time-window of several days or ever longer scales can still work. Then, we also checked the hydrological and rainfall events during a ±7 days' time window. Further, we combined all the available in situ datasets and randomly separated them into two groups, with around 2/3 of the datasets employed for calibration and 1/3 for validation, respectively. More details can be found in the Supplementary Materials.

3.4. Lake Optical Clustering for Rhown(λ)-Spectra

CLMS uses the global set by Spyrakos et al. (2018) for OWTs. Many of the OWTs in this global classification are not present in China. Therefore, we had to develop our own OWT scheme. The lake OWTs included two main steps. The *rhown*(λ)-spectra at 443, 490, 560, 665, 704, and 740 nm were clustered using a k-means approach to match in situ observations. For k-means clustering, a Schwartz Bayes criterion (SIC) was used to determine the statistically optimal number of clusters to identify significant differences ($p < 0.001$) (Table S2). For each new OWT, a different turbidity model was calibrated and validated. For 10 m turbidity mapping, with our turbidity models, we developed a slope threshold approach applied to every water pixel in a hard classification. We first screened the correlations between in situ turbidity measurements with *rhown*(λ)-spectra to find sensitive bands responding to the in situ turbidity levels (See Section 4.2). Further, the slopes of linear fitted sensitive *rhown*-bands (665, 704, and 740 nm) were acquired. The median values of these slopes were considered a threshold for the selection of turbidity models for different OWTs. Eventually, the developed turbidity models matching different OWT configurations were applied to acquire national-scale turbidity products (Figure 2). In order to feasibly add our developed turbidity model, we added about 12 Hydrolight simulation reflectance data with high turbidity levels (ranging from 204.47 NTU to 282.74 NTU).

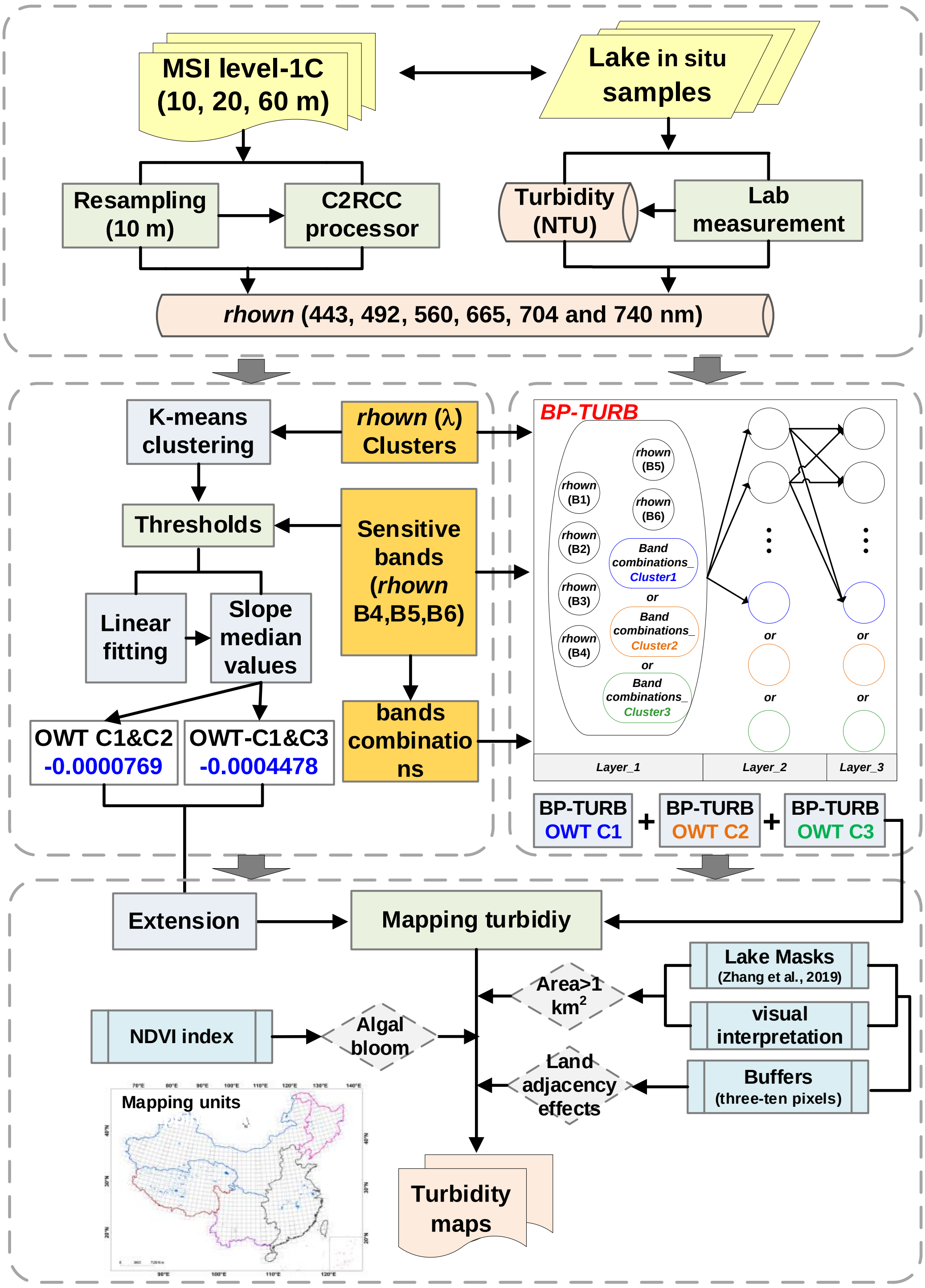

Figure 2. Flowchart of mapping procedures for the Sentinel−2 MSI data preprocessing, k−means *rhown*−spectra clustering, and BP−TURB models.

3.5. Back-Propagation Neural-Turbidity Models (BP-TURB)

As in most neural network algorithms, the BP was based on a multilayer perceptron consisting of several artificial neurons, including the input layer, a hidden layer, and the output layer. It is a flexible algorithm for modeling water quality from remote sensing imagery. We first used a weighted linear summation and bias to connect neurons between every two layers, followed by a nonlinear activation function. If the output values are inconsistent with the desired values, the BP algorithm becomes one of back propagation. The output values are transmitted back to the input layer, and errors are allocated to each neuron of the network. More importantly, we introduced some sensitive *rhown*-bands (665, 704, and 740 nm) that responded to turbidity concentrations for our pooled datasets. As a result, each error signal, which is a prerequisite of revising the weight value between every two neurons, was obtained. The output layer transforms values into the desired water quality indicator (turbidity) (Figure 2). The BP modeling procedure was processed using the Python 3.8 software scikit-learn. The accuracy assessments of the models used correlated coefficients and errors and are shown in the Supplementary Materials).

3.6. Chinese Turbidity Products

Zhang et al. (2019) [19] reported multi-decadal numbers, locations, and distributions of lakes (1960s–2020, 5-years intervals) with Landsat images (Figure S2). We referred to these lakes' numbers, as these can be used as the reference standard for our turbidity products. Lake boundaries were used to extract turbidity maps processed from the MSI satellite data. MSI imagery covering the whole country was used to generate the turbidity products of Chinese lakes. A total of 1234 images (2015: 582 scenes; 2020: 652 scenes) were processed using the C2RCC processor and our BP-TURB models to create the nationwide turbidity maps (Figure 2). Once the annual mean turbidity maps were generated, the average value for all pixels within a lake was estimated during the observation period (2015, 2020). The dynamics of turbidity over temporal (5-year) and spatial (five lake zones) scales were examined. This included changes in the average turbidity, trend, number, and surface area of lakes. As determined by a natural break's method, all lakes (surface area >1 km^2) across China were categorized into six levels: <10 (clear), 10–15 (lightly clear), 15–20 (moderately clear), 20–30 (moderately turbid), 30–45 (very turbid) and 45+ NTU (extremely turbid). More details of data processes are shown in the Supplementary Materials.

3.7. Data on Abiotic Factors

Across large spatial scales, biotic factors and their correlates are pivotal determinants of lake biogeochemistry (Table S3); this is in contrast to the dominance of biotic factors (e.g., eutrophication) in individual lakes [38]. The average depths and lake volumes in millions of cubic meters were gathered from HydroSHEDS datasets, which were estimated using the geostatistical modeling approach [39]. The average lake depth was defined as the ratio between total lake volume and lake area [40]. For natural factors, we considered elevation, climate, vegetation coverage, etc. Elevation was determined from a digital elevation model obtained from the Shuttle Radar Topography Mission (30 m $\times$ 30 m). We extracted the annual mean wind speed recording as m s^{-1} approximately 10 m above the surface of lakes from the European Centre for Medium-Range Weather Forecasts. Likewise, the annual temperature (°C) and precipitation (mm) were gathered from the Resource and Environmental Science and Data Center (RESDC), along with the yearly mean normalized difference vegetation index (NDVI), representing the greening of limnetic regions. These data were averaged considering five lake regions, consistent with mapped turbidity. Finally, anthropogenic factors such as GDP and population data for 2020 were also from RESDC with a 1 km resolution. We also checked the datasets manually. More details of sources of abiotic factor datasets are shown in the Supplementary Materials.

4. Results

4.1. The Importance of Multi-Spatial-Temporal In Situ Water Qualities

In situ and Hydrolight dataset turbidity ranged from 0 to 282.74 NTU, averaging at 39.19 NTU with large spatial variation (standard deviation = 31.12) (Table 1). A total of 33.36% of samples had turbidity greater than 11 NTU, defined as very turbid waters according to the IOCCG report [41]. The average pH and EC (conductivity) were 8.51

(Table 2) and 3252.3 µS cm^{-1}, respectively; SDD and SPM were 1.60 m and 15.77 mg L^{-1}; Chl-a and TP were 7.56 µg L^{-1} and 0.16 mg L^{-1}, respectively. Comparatively, a little bit higher standard deviation could be observed in the EC, turbidity, Chl-a, SPM, and TP concentrations, with a high abundance of water qualities from different lakes. The averaged a_{p} (443), a_{ph}(443), a_{d}(443), and a_{CDOM} (443) were 1.41 m^{-1} (±1.76), 0.48 m^{-1} (±0.72), 0.93 m^{-1} (±1.43), and 0.54 m^{-1} (± 0.43), respectively. Further, there were significant correlations between turbidity and SPM (Table S4; r = 0.88, R^2 = 0.78, p < 0.001), a(443) (r = 0.81, R^2 = 0.66, p < 0.001), and a_{d}(443) (r = 0.80, R^2 = 0.66, p < 0.001), respectively (Figure S3).

Table 1. Descriptive statistics analysis of water qualities of in situ lakes across China.

Parameters	*N*	Avg.	SD.	Min.	Max
Turbidity (NTU) +	484	39.19	31.12	0	282.74
pH	431	8.51	1.04	6.86	13.05
EC (µS cm^{-1})	431	3252.3	6739.31	0.17	33,453.10
SDD (m)	431	1.60	1.50	0.17	9.47
SPM (mg L^{-1})	484	15.77	21.00	0.24	147.50
Chl-a (µg L^{-1})	431	7.56	11.28	0.13	100.22
TP (mg L^{-1})	431	0.16	0.42	0.003	2.17
a_{p}(443) (m^{-1})	431	1.41	1.76	0.01	8.06
a_{ph}(443) (m^{-1})	431	0.48	0.72	0	5.33
a_{d}(443) (m^{-1})	431	0.93	1.43	0	6.96
a_{CDOM}(443) (m^{-1})	431	0.54	0.43	0	1.89

SDD, SPM, Chl-a, and TP are water clarity, suspended matter, chlorophyll-a, and total phosphorus, respectively. + The turbidity levels are considered the Hydrolight simulation data.

4.2. Lake Optical Water Types Clustering

Figure 3 shows the *rhown*(λ)-spectra from atmospherically corrected MSI products. According to our analysis, the *rhown*(λ) was optimally divided into three OWTs (i.e., OWT C1, OWT C2, and OWT C3) when the variation and distance measurement ratios of the SIC were the largest (0.130 and 4.983, respectively). The average *rhown*(λ) result shows that the OWT C3 dataset has relatively high reflectance, with OWT C1 and OWT C2 having progressively lower reflectance. There were notable differences (ANOVA, p < 0.001) in water properties, e.g., pH, SPM, TP, SDD, a_{CDOM}(λ), a_{ph}(λ), and a_{d}(λ) for each partition of *rhown*(λ), followed by EC (p < 0.05) among the OWTs. The optical properties and concentrations of optically active substances, as expected, underpinned the clustering of *rhown*(λ). A literature review to identify spectral bands for turbidity modeling showed that bands and band ratios in the red or NIR wavelength were commonly utilized [42]. Our correlation analysis (r > 0.80, R^2 > 0.62) also indicated that *rhown*(665, 704, and 740 nm) explained a high proportion of turbidity variance (Figure S4).

Thus, we obtained the median values of *rhown* (665, 704, and 740 nm) for integrated OWT C1 and OWT C3 reflectance and integrated OWT C1 and OWT C2 reflectance. Then, a linear fit was determined from the three sensitive bands considering different integrated datasets, aiming to find segmental boundaries among different OWTs. Two slope thresholds (−0.0000769 for OWT C1 and OWT C2; −0.0004478 for OWT C1 and OWT C3) were delineated for turbidity models responding to optical lake types. Given the specific boundaries of different OWTs of stochastic imagery data responding to the turbidity variations, consistent turbidity models and downstream product generation can be conducted.

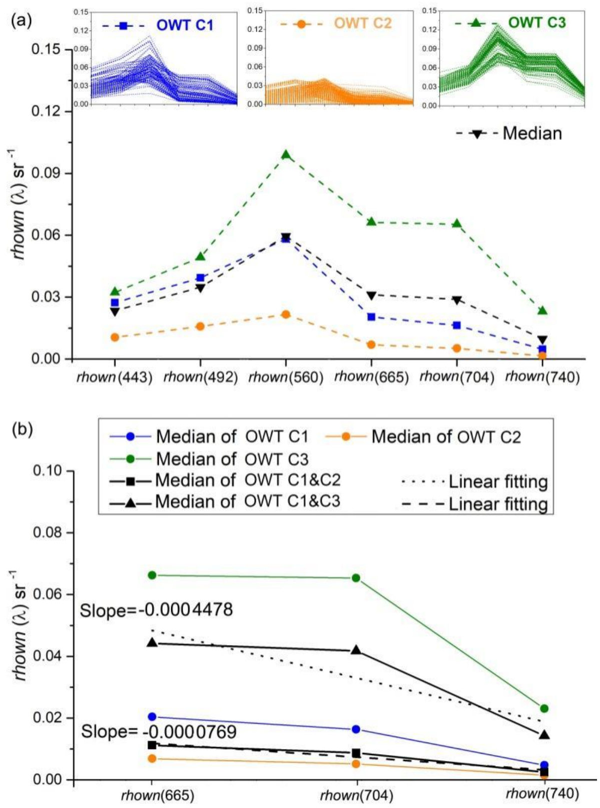

Figure 3. (**a**) The *rhown*(λ) −spectra were divided into OWT C1 (blue line), OWT C2 (orange line), and OWT C3 (green line) by the k−means method and their medians; (**b**) linear fitting for *rhown* (665, 704, and 740 nm) and their slopes with different k-mean clusters.

4.3. BP-TURB Models

A neural net was trained for each OWT by *k*-means clustering schemes and iterative analysis. The model performed well, as seen from the calibration and validation results, the small *y*-intercept and errors, and the close relationships between in situ-measured and MSI-estimated turbidity (high R^2, slope close to 1; Figure 4). When we used *rhown* (443, 490, 560, 665, 704, 740) as the input for OWT C1, the BP-TURB OWT C1 model performed the best, with slopes close to 1 (slope > 0.83), and returned a high $R^2 > 0.87$ (Table 2). We used iteration to select the sensitive bands or band combinations responding to the turbidity concentrations for the following OWTs. The band levels were ranked according to maximum Pearson coefficient (*r*, 2-tailed, $p < 0.01$), denoting the best correlations with turbidity, and were assigned in the algorithm configuration optimization using the BP neural network as input variables. For the OWT C2 dataset, there were 13 bands or band combinations used as input variables for BP-TURB OWT C2, performing well (slope > 0.82 and $R^2 > 0.81$).

Table 2. The input variables of BP-TURB models considering different OWTs and their performances compared with multiple linear regression between measured and estimated turbidity from the MSI spectral bands for a pool dataset (unit: NTU).

Models	Input Band Combinations or Model	Datasets	*N*	Slopes *	R^2	Errors
BP-TURB OWT C1	Input: *rhown* (443, 490, 560, 665, 704 and 740)	Cal-	76	0.84	0.87	RMSE = 4.01; MAE = 2.99
		Val-	39	0.83	0.88	RMSE = 4.42; MAE = 3.00
BP-TURB OWT C2	Input: *rhown* (443, 490, 560, 665, 704 and 740); *rhown* (665 × 704 × 740/443); *rhown*(560 × 704 × 665/443); *rhown*(704 × 740/490); *rhown*(704 + 740/443); *rhown*(704+740/560); *rhown*(665 + 704 + 490/443); *rhown*(704 × 740)	Cal-	163	0.83	0.81	RMSE = 3.24; MAE = 2.51
		Val-	82	0.82	0.81	RMSE = 3.67; MAE = 2.91

Table 2. *Cont.*

Models	Input Band Combinations or Model	Datasets	*N*	Slopes *	R^2	Errors
BP-TURB OWT C3	Input: *rhown* (443, 490, 560, 665, 704 and 740); *rhown*(704 × 740/490); *rhown*(665 × 704/490); *rhown*(704 × 740/665); *rhown*(560 × 740/443); *rhown*(490 × 665 × 704/443); *rhown*(665 × 704 × 740/443); *rhown*(560 × 740/443); *rhown*(665 × 704/443); *rhown*(704 × 740/443); *rhown*(490 × 704 × 740/443); *rhown*(490 × 740/443); *rhown*(704 × 740)	Cal-	131	0.87	0.79	RMSE = 27.74; MAE = 20.92
		Val-	64	0.89	0.81	RMSE = 17.54; MAE = 11.20
Multiple Linear regressions	Input: *rhown*(740) Cal-:*Tur* =2059.14 × *rhown*(740) + 0.669	Cal-	370	-	0.56	RMSE = 14.96; MAE = 8.02
	Val-:$Tur_{estimated}$ = 0.63 × $Tur_{measured}$ + 7.18	Val-	185	0.63	0.53	RMSE = 15.12, MAE = 8.12
	Input: *rhown*(709), *rhown*(740) Cal-:*Tur* = 6867.67 × *rhown*(740)–1752.26 × *rhown*(709) + 3.96	Cal-	370	-	0.55	RMSE = 27.20; MAE = 17.36
	Val-:$Tur_{estimated}$ = 0.64 × $Tur_{measured}$ + 6.87	Val-	185	0.64	0.55	RMSE = 48.60; MAE = 30.11,

* Slopes of linear fitting, where a slope close to 1 represents the unbiased performance of models. Cal- represents the calibration dataset, and Val- was validation dataset. $Tur_{estimated}$ and $Tur_{measured}$ represent the estimated and measured turbidity for our lake samples.

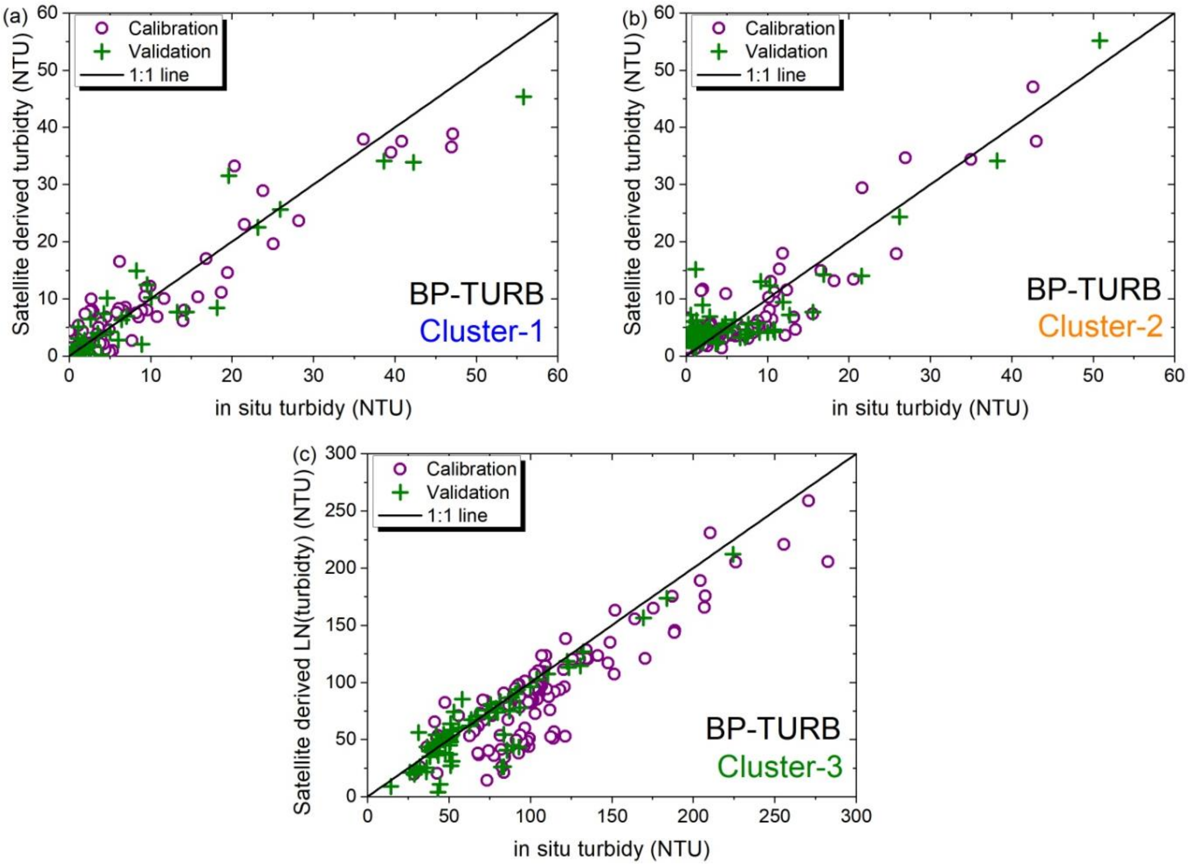

Figure 4. Relationships between measured and estimated turbidity for BP-TURB models' calibration and validation datasets, of which (**a**) is the BP-TURB OWT C1 model, (**b**) is BP-TURB OWT C2 model, and (**c**) BP-TURB OWT C3 model, respectively.

Further, our trial analysis found that the turbidity model for the OWT C3 dataset can have improved performances when a total of 18 bands or band combinations (moderate correlations, $r > 0.55$) are joined and developed as BP-TURB OWT C3 (Table 2). The synergistic BP-TURB models with the *k*-means clustering of reflectance can be applied to provide a reliable framework to estimate turbidity and to generate national-scale turbidity products.

4.4. Spatial Distributions of Turbidity in 2015 and 2020

Figure 5a shows the distributions of lake turbidity in the five lake zones across China in 2015 and 2020, revealing remarkable spatial variations, with plateau lakes generally having lower turbidity than plain lakes. A larger percentage of clear lakes (53.26%) with low turbidity levels (<10 NTU) was found in 2020 than in 2015 (37.43%). Likewise, 7.78% of lakes were moderately clear, 8.51% were moderately turbid, and 8.74% were very turbid in 2020, exhibiting significant improvement compared to 2015 (11.16%, 17.03%, and 12.57%), respectively. There were significant differences among different limnetic regions from different years (F = 48.3 and 54.53, $p < 0.001$) (Figure 5). For annual mean turbidity (NTU) in 2015 and 2020, the top regions were NLR (26.59, 29.54), ELR (20.44, 15.42), and MXR (21.79, 18.41), followed by TQR (15.24, 13.69) and YGR (10.61, 16.80). The lakes with turbidity >45 NTU were most common and accounted for 13% (NLR), 6% (ELR), 18% (MXR), 8% (TQR), and 5% (YGL) in 2015, consistent with results of 26%, 6%, 11%, 7%, and 12% in 2020, indicating that NLR has the highest lake abundance with extreme turbidity (Figure 5d). Lake turbidity values showed obvious improvements in this 5-year comparison, considering the intermediate turbidity levels (very turbid, moderately turbid, and moderately clear). Turbid lakes (>30 NTU) were common over Songnen Plain (NLR), Xilinguole (MXR), and Shanxi Province (MXR), as well as in YGL. Conversely, a larger percentage of lakes had low turbidity in the Yangtze River basin flat plains (ELR).

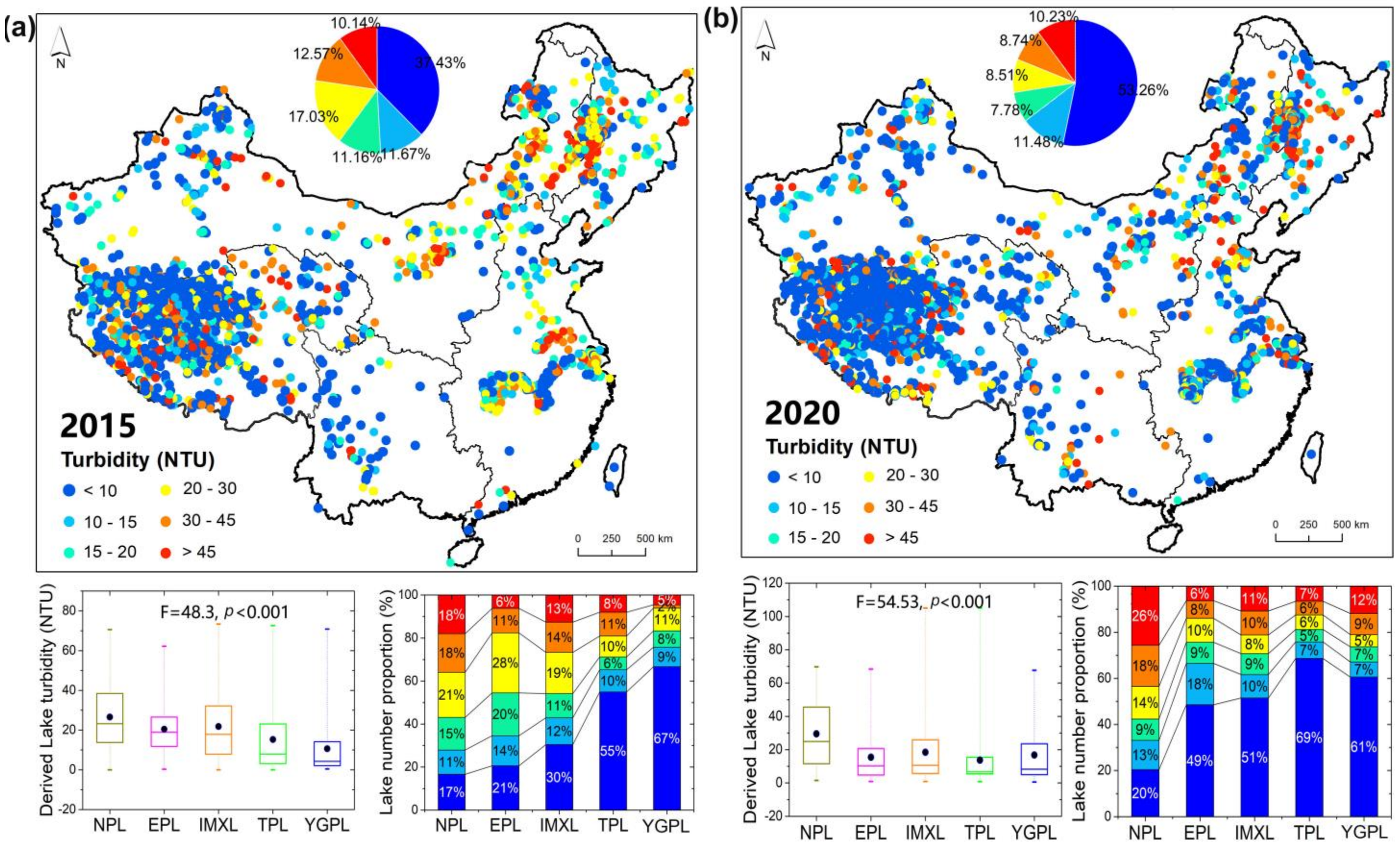

Figure 5. The mean turbidity (NTU) of lakes (>1 km^2) across China in 2015 (**a**) and 2020 (**b**) from our BP-TURB models, respectively, and their spatial distribution of lakes with mean turbidity, proportion of lake number with turbidity values for six different levels, box plots of the mean turbidity values, and proportion of lake number at different turbidity levels from the five limnetic regions.

4.5. Temporal Dynamics of Lake Turbidity (>1 km^2)

4.5.1. Temporal Average and Trend in Lake Turbidity

Turbidity ranged from 0.01 to 98.63 NTU with an average of 19.35 ± 8.70 NTU in 2015; turbidity ranged from 0.01 to 122.09 NTU with a mean of 16.92 ± 6.25 NTU in 2020. There were significant differences (F = 27.74, $p < 0.001$) in lake turbidity between the two studied years. The NLR showed the highest lake turbidity, with an average turbidity of 26.6 ± 16.56 NTU (2015) and 29.54 ± 19.83 NTU (2020), followed by lakes of MXR (2015, 21.79 ± 16.51 NTU; 2020, 18.41 ± 17.65 NTU) and ELR (2015, 20.44 ± 12.55 NTU; 2020, 15.42 ± 14.77 NTU), while turbid lakes mostly dominated in the flat plains (Figure 6). Mean turbidity values of lakes in TQR (2015, 15.24 ± 16.04 NTU; 2020, 13.69 ± 14.96 NTU) and YGR (2015, 10.61 ± 14.86 NTU; 2020, 16.80 ± 17.94 NTU) located at high altitudes (Tibet Plateau and Yungui Plateau) had high spatial heterogeneity and were relatively low.

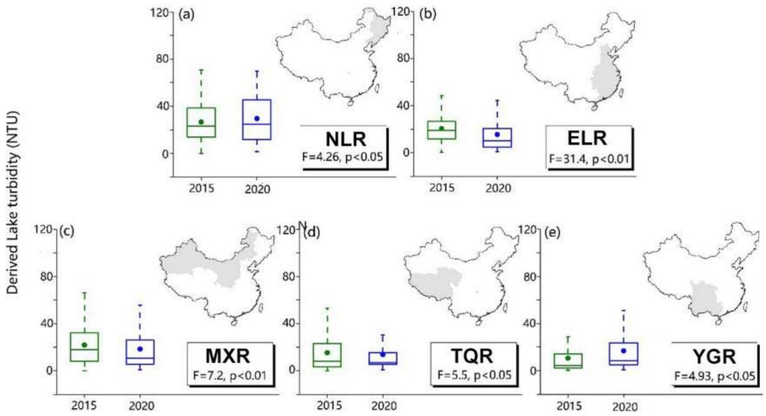

Figure 6. Box plots of turbidity in several lakes from the five limnetic regions, i.e., (**a**) NLR, (**b**) ELR, (**c**) MXR, (**d**) TQR, and (**e**) YGR, and ANOVA analysis (significance, $p < 0.05$).

4.5.2. Interannual Changes in Turbidity

While assembling the datasets for this study, lakes, such as Chagan Lake (NLR), Hulun Lake (MXR), Taihu Lake (ELR), Qinghai Lake (TQR), and Dianchi Lake (YGR), were mapped with our BP-TURB models (Figure 7 and Table S5). In Taihu Lake, the highest turbidity occurred in spring (26.18 NTU), followed by summer (13.36 NTU), and spring (23.28 NTU). Due to high elevation and less human activity, Qinghai Lake had lower average turbidity, with the following seasonal variations: 13.05 NTU (spring) >11.36 NTU (summer) > 8.48 NTU (autumn). The same seasonal dynamics were held for Dianchi Lake (16.12 NTU, 10.32 NTU, and 11.64 NTU). The seasonal averaged turbidity of Hulun Lake was 40.11 NTU (spring) > 36.57 NTU (summer) > 17.50 NTU (autumn), suggesting terrestrial inputs via soil leaching and runoff in spring. Evidently, Chagan Lake has stable seasonal dynamics for lake turbidity, with average turbidity values greater than 30 NTU. The dynamic processes of lake turbidity are affected by the regional environmental background, e.g., hydrology, climate, and anthropogenic activities, over large-scales.

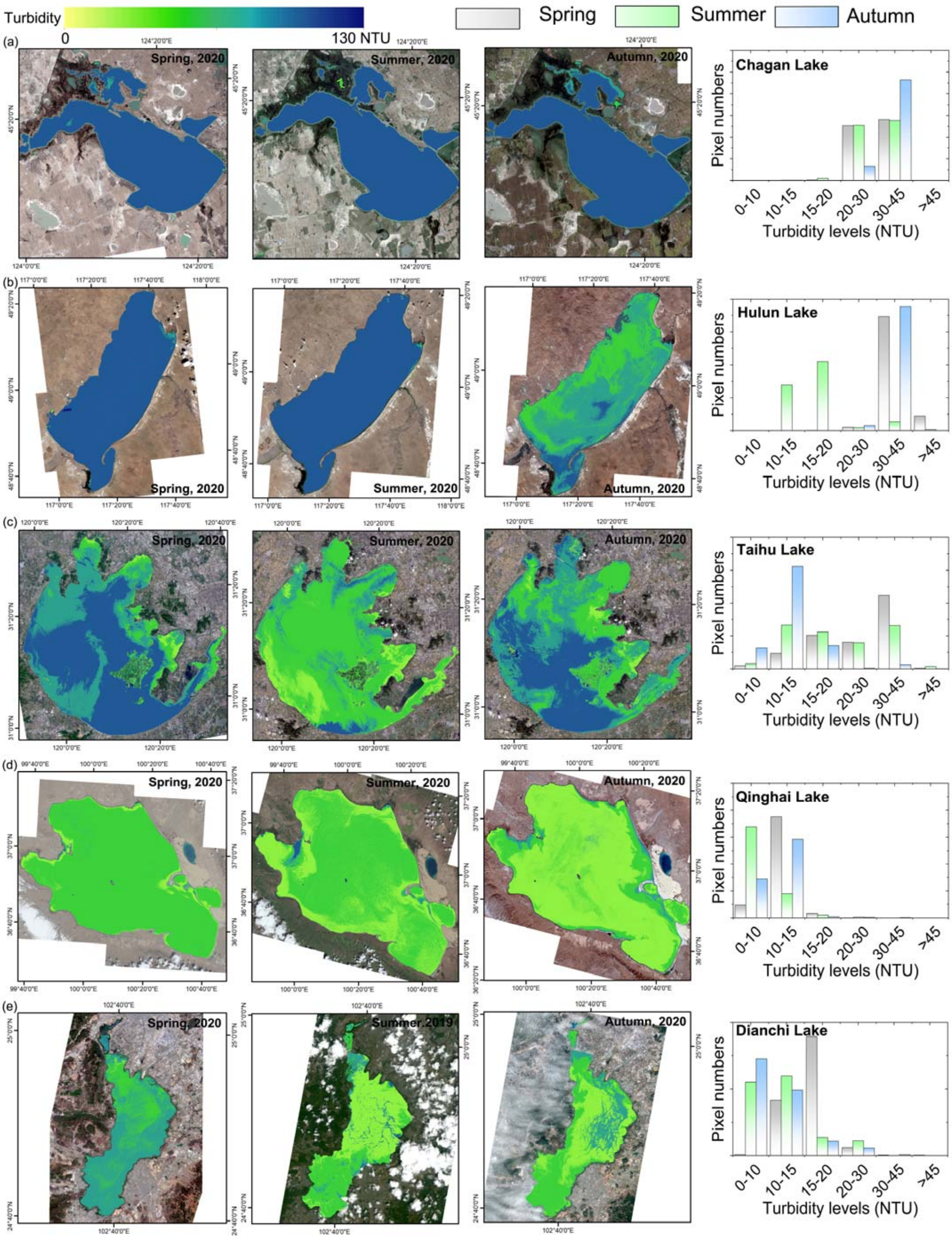

Figure 7. Spatial variations of turbidity derived from BP-TURB models in typical lakes, e.g., (**a**) Chagan Lake, (**b**) Hulun Lake, (**c**) Taihu Lake, (**d**) Qinghai Lake, and (**e**) Dianchi Lake, and their pixel numbers in different turbidity ranges. For each lake, the seasonal turbidity dynamics were mapped within spring (April to May), summer (June to August), and autumn (September to October).

4.6. Abiotic Factors Acting on the Spatial Variations of Turbidity

Lake turbidity was considered to be co-determined by various abiotic factors [24,43]. Satellite-derived average turbidity for all lake pixels in 2020 was used to represent the turbidity levels across China. Within a specific lake zone, turbidity varied spatially. Then, the consistent spatial variations of abiotic factors, such as lake characteristics, natural factors, and anthropogenic factors, also showed different distributions among five limnetic regions (Table S1 and Figure 8a). For Chinese lakes (area >1 km^2) in 2020, there was a moderately negative correlation between average turbidity and elevation, with $R^2 = 0.52$ ($p < 0.05$) (Figure 8b). Likewise, the derived turbidity by BP-TURB models showed that the average turbidity was strongly negatively related to lake volume ($R^2 = 0.86$, $p < 0.01$), as well as moderately correlated with lake average depth ($R^2 = 0.56$, $p < 0.05$). Meanwhile, BP-TURB models revealed a strong negative relationship between average turbidity and lake volume ($R^2 = 0.86$, $p < 0.01$), as well as a modest relationship with lake average depth ($R^2 = 0.56$, $p < 0.05$). Multiple abiotic factors influenced turbidity in Chinese lakes, with the geographical distributions of turbidity being mainly influenced by lake volume, followed by lake depth and elevation.

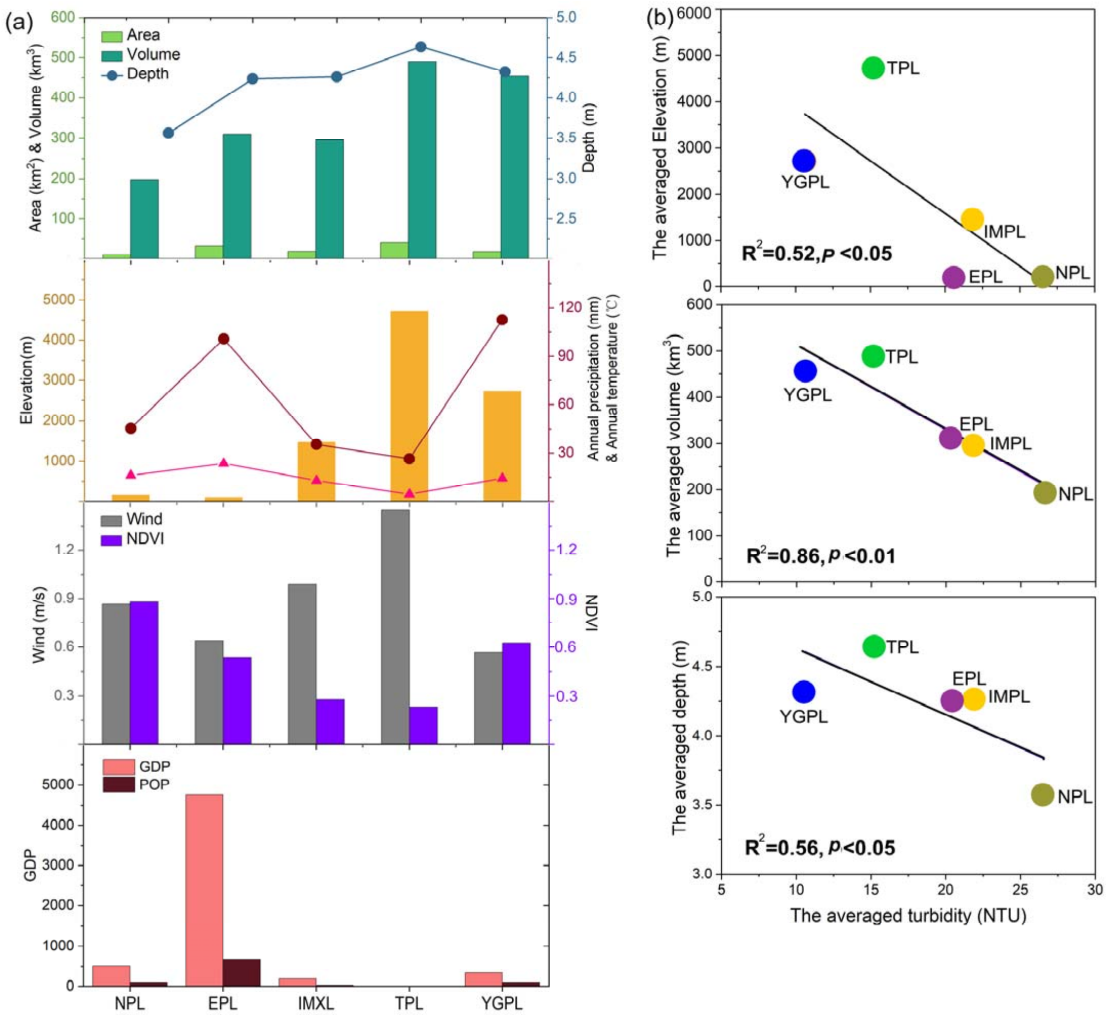

Figure 8. Average values of abiotic factors (**a**), i.e., lake characteristic factors, natural factors, and anthropogenic factors (Table S1), and regression analysis (**b**) among turbidity, lake volume, lake average depth, and elevation in five limnetic regions.

5. Discussion

5.1. OWTs Clustering for Turbidity Modeling

The efforts [28] to increase the usage of remote sensing in monitoring biogeochemical characteristics and processes taking place in lakes have increased considerably (e.g., Chl-a, and CDOM; IOPs, absorption; radiometric quantities) [44]. However, several studies have shown that it is difficult to develop a universal algorithm for such a variety of lakes [30]. On the other hand, if such an algorithm is developed, then it often performs poorly for every lake separately (Table 2). Remote sensing algorithms are not universal and need tuning for specific lakes. Although the specific tuning of remote sensing algorithms of lakes could improve derived results locally, these would be not appropriate for studies of large-scale regions. Water pixels, on the other hand, are snapshots of a continuum that represent average optical conditions. Nevertheless, the pure water pixels near the shore are affected by complex processes linked to adjacency effects or shallow bottom, resulting in a higher variance in turbidity estimation. Based on the obvious differences in spectral shapes and the magnitude of reflectance or radiometric quantities, water optical typologies allow us to capture the unique characteristics of lakes [44]. Clustering OWTs before mapping turbidity is a good compromise to develop groups of optimized algorithm configurations with lower variance. This process did not require preliminary parameterization data (e.g., suspended matter, trophic state, etc.) to improve the performance of models [16]. As illustrated in Tables 2 and S6, the turbidity levels and optically active constituents for each class were different, with significant differences among turbidity, SPM, and $a_{\mathrm{d}}(443)$ ($F > 170.4$, $p < 0.000$). It can be inferred that lakes in OWT C3 were turbid with higher SPM and Chl-a, and lakes in OWT C2 were clear. We developed two empirical algorithms based on all in situ datasets we had (Table S5) in order to compare how the OWT-assisted neural network performed compared to that of the conventional approach. The results are provided in Figure 4 and bands or band combinations in Table 2. OWT-assisted BP-TURB models outperformed previously proposed empirical algorithms. Despite the great variability of these in-water characteristics and the often-complex interactions between reflectance and water qualities, there are some notable differences for different OWTs (Table S2). As expected, the optical properties (e.g., $a_{\mathrm{d}}(443)$, $a_{\mathrm{ph}}(443)$, and $a_{\mathrm{g}}(443)$) and SPM underpin the clustering of *rhown*-bands, with significant differences (AVOVA, $p < 0.001$) (Table S2). There were no significant differences in Chl-a among different OWTs, owing to the dominance of suspended matter on measured turbidity levels. For turbidity product generation on a national-scale, we adopted a new approach of assigning pixels or observations to the optimized algorithm configuration scheme by OWTs (Figure 2).

5.2. Remotely Sensed Turbidity Models

There is evidence [15,16,18,45] that, despite that sentinel MSI was built as a land sensor, it can be used for water remote sensing as well. In situ turbidity measurements showed significant correlations with *rhown*(665), *rhown*(704), and *rhown*(740) ($p < 0.001$) (Figure S4). The reflectance signals in the red bands were jointly modulated by optically active substances and varied within different lake characteristics and watershed catchments [30]. The correlation between the reflectance values and optical water constituents was purely due to optics. Band ratio algorithms are the most primitive way to relate optical water properties (reflectance) and other water properties. In general, the broader MSI bands have increased sensitivity to the integrated absorption and scatter properties of optically active substances (e.g., Chl-a, SPM, and CDOM), signifying turbidity (this study), or in other studies, trophic state [18,45]. Matsushita et al. (2015) [46] also demonstrated that quantifying water qualities in turbid waters generally requires a sufficient signal to noise ratio at red or NIR bands. Turbidity is always a relative measurement, comparing how much light a sample scatters to how much light a standard scatters. The turbidity of the sample increased as more light was scattered. Simultaneously, the turbidity was driven primarily by SPM or phytoplankton scatter within reflectance, and suspended solids had strong backscattering at red or NIR wavelengths [36]. Because particles dominate the optical properties of our investigated waters, turbidity generally showed significant correlations with SPM (Figure S3). The turbidity products (e.g., Copernicus Global Land Service) are therefore frequently derived from SPM models. However, these products are for Europe and Africa and are not available in China. Likewise, the OWTs (see Section 5.1) and calibrated datasets should be based on wide ranges of turbidity levels. While encouraging, the BP-TURB by MSI sensor considering OWTs was developed (Figure 4). A blended algorithm approach is superior to single algorithms when considering the entire dynamic range of environmental conditions.

Machine learning algorithms are superior at dealing with high-dimensional and nonlinear regression problems [11]. They are excellent for solving the nonlinear relationships between reflectance and in situ turbidity, considering moderate and even high turbidity. However, if we considered OWTs for every pixel in an investigation of large-scale lake groups with moderate or small lakes, this process would be time-consuming (Figure 4, Table S4). BP integrated across sensitive bands of turbidity performed better than either of the relatively coarse and poorly generalizable empirical models. Likewise, BP always has a baby-size computational overhead compared to other machine learning algorithms (e.g., support vector machines). Our trial analysis found that the BP-TURB model for the OWT C3 dataset required more band combinations responding to in situ turbidity as input variables (Table S6). This caused algorithm performance to improve across the entire training dataset (CAL and Val version).

As illustrated in Table 2, OWT C3 waters typically had relatively high SPM (OWT C3, 43.2 mg $L^{-1} \pm 23.2$) and Chl-a (OWT C3, 9.2 μg $L^{-1} \pm 8.4$) coupled with non-covarying OACs ($a_d(443)$, 2.43 $m^{-1} \pm 1.85$) compared to OWT C1 and OWT C2 waters. The fact that *rhown*(λ) can vary with changing optically active substances is shown in Figure 3. For example, the variance of particulate concentration and particle assemblage from 0.1 to 2 μm can efficiently increase the scattered light, reflecting in the reflectance spectral dependency [36]. Likewise, the non-covarying OACs ($a_d(443)$ and $a_{CDOM}(443)$) had a significant impact on the reflectance at blue or green spectral bands [47]. In addition to predictive performance, BP-TURB OWT C3 exhibited good performance.

5.3. Chinese Lake Turbidity Distributions in Five Limnetic Regions

Early investigations of Chinese lake turbidity were conducted in regional lake groups located in the Middle and Lower Yangtze River basin [20] and in Poyang Lake [22]. Many studies or monitoring agencies used a relative parameter turbidity to actually represent a concentration of SPM, as turbidity measurements are less time consuming and much cheaper. (Section 5.2). No systematic efforts have been made to establish a long-term record of water turbidity data for a large-scale Chinese lake overview. This study is the first attempt to achieve this. Although turbidity varied spatially within lake regions, low turbidity lakes were mostly located in the southwest plateau regions such as Tibet (TQR) and Yunnan-Guizhou (YGR) (Figure 5). Our results were consistent with the spatial distributions of lake clarity demonstrated from Song et al. (2021) [48]. They also showed that lake clarity was high in TQR and YGR.

The abiotic factor analysis indicated that satellite-derived turbidities were mainly a function of lake volume, followed by lake depth, and elevation (Figure 8b). This is not surprising, as turbidity is usually higher in shallower and smaller lakes due to resuspension. For example, mineral particles settle out from the water column relatively quickly. If the lake is deep (and consequently the volume is large), then these particles cannot re-suspend and are out of circulation. In shallow lakes, the turbidity is high. Theoretically, lake turbidity is co-determined by phytoplankton, suspended matter, and CDOM [49]. Increased phytoplankton means higher turbidity. Thus, there should be good correlation between Chl-a and turbidity, not observed in our in situ data. Consequently, mineral particles dominated in the formation of turbidity, e.g., SPM. High CDOM (yellow substances) may reduce turbidity values due to the absorption of light [50], meaning that the measured turbidity In CDOM-rich lakes can be lower, not because there are less scattering particles, but because some of the light traveling between the light source and sensor is absorbed. However, the CDOM concentrations in the lakes studied were relatively small and should have had little effect on turbidity measurements that were carried out at 680 nm. In contrast, the abiotic factors we studied (Table S3) and their correlates are pivotal factors in determining lake biogeochemistry at multiple scales [38]. This could help to understand the mechanistic processes governing specific lake water qualities, optical absorption processes, and spectral clustering (Sections 5.1 and 5.2). However, a large-scale study of abiotic factors' (list in Table S3) influence on lake turbidity is required to understand the future prospects of lakes in response to global changes. For example, increased turbidity from a climate-driven increase in sediment re-suspension can be associated with the erosion of recently submerged shorelines following submersion during the rapid expansion of a lake [51].

In comparison to our finding (Figure 8b) that increased lake volume was significantly negatively correlated with lake turbidity, high water level could contribute to weak sediment re-suspension, stable water flow conditions [22], and good buffer capacity. Previous studies [43] have demonstrated that lakes with mean depths >5 m in China are mainly located in the YPL, IMXPL, and TQR, whereas the lakes located in the ELR had a mean water depth of only 3.42 m. These lakes are hydro-geographically connected with the rivers, and their turbidity values are controlled by the re-suspension of sediments [52]. In addition, our results also showed that distributions of lake elevation were negatively correlated to lake turbidity in five limnetic regions. We suspected that two interactive factors, such as elevation and anthropogenic activities, drive turbidity, possibly by increasing available nutrients from agricultural and sewage discharge and runoff from the surrounding land, which in turn impacts soil erosion. Although we analyzed the effects of abiotic factors on lake turbidity, it should be emphasized that lake volume dominated.

5.4. Comparison with Past Studies, Uncertainties, Challenges, and Future Perspectives

Observing lake water qualities with MSI is not without challenges [15]. Recognized challenges include issues related to atmospheric correction [37], land adjacency effects [53], and bottom reflectance [54]. In our study, we aimed to provide technical operations and downstream products; the dedicated processes can be either seen as: (i) C2RCC processor, (ii) k-means clustering of reflectance for developing new BP-TURB models, (iii) clustering schemes for mapping, (iv) buffers approximately 3–10 water pixels for lake masks, and (v) removing the area of algal bloom, to reduce the errors from atmospheric correction (e.g., aerosol characterization) and mixed pixels caused by land adjacency and shallow lake bottom reflectance. Our in situ turbidity ranges for developing the models varied from 0 to 282.74 NTU, covering wide ranges from clear to turbid lakes. Nevertheless, our ambition for this work was to provide a novel OWT and BP framework, which could lead to more targeted validation efforts. Note that we referred to Song et al., (2020, 2022) [32,48] to select the appropriate MSI images with a 7-day time window. This was due to the limited image numbers in low-latitude regions compared to those in high-latitude regions, and Toming et al. (2016) [15] and Cardille et al. (2013) [55] found that, in some cases, even longer (weeks to month scale) time differences may still be acceptable. We compared the model performance of BP-TURB considering different time windows (Figure S5). It can be seen that the BP-TURB C1 and BP-TURB C3 models showed relatively significant performances, with a high linear fitting slope and R^2 found in the longer $\pm$0–1 day time-window. However, for the BP-TURB C2 dataset, we found there was no significant improvement. In addition, the BP-TURB models, including other machine learning algorithms, are data-driven models, and their performance largely depends on sample size and the importance of each feature band. More effort can be made for in situ collection and the development of other machine learning algorithms of turbidity when adding more sensitive band combinations. Reparametrizing model inputs considering targeted water types specifically could improve performance across the turbidity concentration continuum. This, due to the lake-specific differences in algorithm performance, will manifest in the algorithm response when its specificity to the target substance is relatively poor. However, the generalization of these methods remains to be demonstrated as robust across OWTs, providing a clearer knowledge of optical behaviors. In a broader sense, the scheme provided here can be used as a template to guide band selections, algorithm selection, and downstream product generation, including for atmospheric correction processors that could be considered within the same OWTs.

6. Conclusions

We proposed a methodology that combines the spectral clustering of optical water types and BP-based models using Sentinel-2 imagery. In situ turbidity data over a diverse range of bio-optical regimes were collected in 2017–2019 and were used to develop BP-TURB models. The high spatial resolution of the atmospheric corrected imagery (10 m) allowed mapping all Chinese lakes that are at least 1 km^2 in size. Complete turbidity maps were generated from Sentinel-2 imagery for two years (2015, 2020) in order to study changes in lakes over the 5-year period, and the abiotic factors acting on the spatial variations of turbidity were examined. Our methodology provided a large-scale application example of lake turbidity. Some findings were acquired from this study as follows:

(1) The *rhown*(λ), consistent with in situ samples, was optimally divided into three OWTs (i.e., OWT C1, OWT C2, and OWT C3) with notable differences (ANOVA, $p < 0.001$) in water properties, e.g., pH, SPM, TP, SDD, $a_{CDOM}(\lambda)$, $a_{ph}(\lambda)$, $a_d(\lambda)$, and EC.
(2) The developed BP-TURB models, including BP-TURB OWT C1, BP-TURB OWT C2, and BP-TURB OWT C3, performed well with slopes close to 1 (slope > 0.82), $R^2 > 0.81$, RMSE < 17.54, and MAE < 11.20.
(3) For Chinese lakes, a larger percentage of clear lakes (53.26%) with low turbidity levels (<10 NTU) was found in 2020 than in 2015 (37.43%). The turbidity patterns were determined by lake volume, average depth, and elevation.

The BP-TURB models were confirmed to have stable performance and temporal transferability. This will allow for using the methodology in routine water quality monitoring, as well as in studying the effects of climate change and anthropogenic pressure on lakes.

Supplementary Materials: The following supporting information can be downloaded at: https://www.mdpi.com/article/10.3390/rs15102489/s1, Figure S1: The DEM, temperature and precipitation GDP, population and land-use distribution maps of China; Figure S2: Chinese lake numbers distributions and proportions in 2015 and 2020. The data from Zhang et al., (2019) and lake boundaries (1960s-2020) have been released by the National Tibetan Plateau Data Centre; Figure S3: The regression analysis of turbidity and SPM (a), $a(443)$ (b) and $a_d(443)$ (c), and the absorption contribution at 443 nm of phytoplankton pigment absorption $a_{ph}(443)$, non-algal particles $a_d(443)$ and CDOM absorption $a_{CDOM}(443)$. The r is Pearson correlation coefficients found in Table S1, and R^2 is regression coefficient, respectively; Figure S4: The regression analysis of *rhown*(λ) and turbidity, (a) *rhown*(443), (b) *rhown*(490), (c) *rhown*(560), (d) *rhown*(665), (e) *rhown*(709) and (f) *rhown*(740), for all data sets. The R^2 is regression coefficient, respectively; Figure S5: The performance of BP-TURB model considering different time-window, e.g., 0-1 days, 0-3 days, 0-5 days and 0-7days; Table S1: Field surveys of lake name, abbreviation, location, and sampling dates of *in situ* lakes across China; Table S2: ANOVA analysis of reflectance spectra *rhown*(λ) according to OWTs (Avg. ± SD.); Table S3: Environmental abiotic factors in China; Table S4: Pearson analysis of water quality parameters from in situ lakes across China; Table S5: The Sentinel-2 A/B Level1C images used to estimate turbidity concentration in typical lakes; Table S6: The description statistic and ANOVA analysis of water quality parameters considering different OWTs. References [48,56–59] are cited in Supplementary Materials.

Author Contributions: S.L. and K.S. designed and performed the study; T.K. and G.L. revised the paper; Y.L. collected in situ data and image processing. All authors have read and agreed to the published version of the manuscript.

Funding: This research was funded by [National Natural Science Foundation of China Fund] grant number [U2243230, 42201414, 42171374, 42071336, 42171385, 42101366, 42201433 and 42001311], the 'Young support talents program' from the Science, Technology Association of Jilin Province (2020–2023) to Dr. Sijia Li and Land Observation Satellite Supporting Platform of National Civil Space

Infrastructure Project (CASPLOS-CCSI). Tiit Kutser was supported by the Estonian Research Council grant (PRG302).

Data Availability Statement: The data presented in this study are available upon request from the corresponding author.

Acknowledgments: The authors thank all staff and students for their persistent assistance with both field sampling and laboratory analysis.

Conflicts of Interest: The authors declare no conflict of interest.

References

1. Lampert, W.; Sommer, U. *Limnoecology: The Ecology of Lakes and Streams*; Oxford University Press: Oxford, UK, 2007.
2. Maberly, S.C.; O'Donnell, R.A.; Woolway, R.I.; Cutler, M.E.J.; Gong, M.; Jones, I.D.; Merchant, C.J.; Miller, C.A.; Politi, E.; Scott, E.M.; et al. Global lake thermal regions shift under climate change. *Nat. Commun.* **2020**, *11*, 1232. [CrossRef] [PubMed]
3. Davies-Colley, R.J.; Smith, D.G. Turbidity Suspended Sediment, and Water Clarity: A Review 1. *JAWRA J. Am. Water Resour. Assoc.* **2001**, *37*, 1085–1101. [CrossRef]
4. Anderson, C.W. Turbidity 6.7. In *USGS National Field Manual for The Collection of Water Quality Data*; US Geological Survey: Reston, VA, USA, 2005.
5. Petus, C.; Chust, G.; Gohin, F.; Doxaran, D.; Froidefond, J.-M.; Sagarminaga, Y. Estimating turbidity and total suspended matter in the Adour River plume (South Bay of Biscay) using MODIS 250-m imagery. *Cont. Shelf Res.* **2010**, *30*, 379–392. [CrossRef]
6. Michaud, J.P. *A Citizen's Guide to Understanding and Monitoring Lakes and Streams*; Publ. #94–149; Washington State Department of Ecology, Publications Office: Olympia, WA, USA, 1991.
7. Jacobsen, L.; Berg, S.; Baktoft, H.; Nilsson, P.A.; Skov, C. The effect of turbidity and prey fish density on consumption rates of piscivorous Eurasian perch Perca fluviatilis. *J. Limnol.* **2014**, *73*, 187–190. [CrossRef]
8. Woolway, R.I.; Merchant, C.J. Wordlwide alteration of lake mixing regimes in response to climate change. *Nat. Geosci.* **2019**, *12*, 271–276. [CrossRef]
9. Dudgeon, D.; Arthington, A.H.; Gessner MO Kawabata, Z.I.; Knowler, D.J.; Lévêque, C.; Naiman, R.J.; Prieur-Richard, A.H.; Soto, D.; Stiassny, M.L.; Sullivan, C.A. Freshwater biodiversity: Importance, threats, status and conservation challenges. *Biol. Rev.* **2006**, *81*, 163–182. [CrossRef]
10. Moore, G.K. Satellite remote sensing of water turbidity/Sonde de télémesure par satellite de la turbidité de l'eau. *Hydrol. Sci. J.* **1980**, *25*, 407–421. [CrossRef]
11. Ma, Y.; Song, K.; Wen, Z.; Liu, G.; Shang, Y.; Lyu, L.; Du, J.; Yang, Q.; Li, S.; Tao, H.; et al. Remote sensing of turbidity for lakes in northeast China using Sentinel-2 images with machine learning algorithms. *IEEE J. Sel. Top. Appl. Earth Obs. Remote Sens.* **2021**, *14*, 9132–9146. [CrossRef]
12. Wang, Y.; Feng, L.; Liu, J.; Hou, X.; Chen, D. Changes of inundation area and water turbidity of Tonle Sap Lake: Responses to climate changes or upstream dam construction? *Environ. Res. Lett.* **2020**, *15*, 0940a1. [CrossRef]
13. Toth, C.; Jóźków, G. Remote sensing platforms and sensors: A survey. *ISPRS J. Photogramm. Remote Sens.* **2016**, *115*, 22–36. [CrossRef]
14. Olmanson, L.G.; Brezonik, P.L.; Bauer, M.E. Evaluation of medium to low resolution satellite imagery for regional lake water quality assessments. *Water Resour. Res.* **2011**, *47*, W09515. [CrossRef]
15. Toming, K.; Kutser, T.; Laas, A.; Sepp, M.; Paavel, B.; Nõges, T. First experiences in mapping lake water quality parameters with Sentinel-2 MSI imagery. *Remote Sens.* **2016**, *8*, 640. [CrossRef]
16. Li, S.; Song, K.; Wang, S.; Liu, G.; Wen, Z.; Shang, Y.; Lyu, L.; Chen, F.; Xu, S.; Tao, H.; et al. Quantification of chlorophyll-a in typical lakes across China using Sentinel-2 MSI imagery with machine learning algorithm. *Sci. Total Environ.* **2021**, *778*, 146271. [CrossRef]
17. Pahlevan, N.; Chittimalli, S.K.; Balasubramanian, S.V.; Vellucci, V. Sentinel-2/Landsat-8 product consistency and implications for monitoring aquatic systems. *Remote Sens. Environ.* **2019**, *220*, 19–29. [CrossRef]
18. Soomets, T.; Uudeberg, K.; Jakovels, D.; Brauns, A.; Zagars, M.; Kutser, T. Validation and comparison of water quality products in baltic lakes using sentinel-2 msi and sentinel-3 OLCI data. *Sensors* **2020**, *20*, 742. [CrossRef]
19. Zhang, G.; Yao, T.; Chen, W.; Zheng, G.; Shum, C.K.; Yang, K.; Piao, S.; Sheng, Y.; Yi, S.; Li, J.; et al. Regional differences of lake evolution across China during 1960s–2015 and its natural and anthropogenic causes. *Remote Sens. Environ.* **2019**, *221*, 386–404. [CrossRef]
20. Hou, X.; Feng, L.; Duan, H.; Chen, X.; Sun, D.; Shi, K. Fifteen-year monitoring of the turbidity dynamics in large lakes and reservoirs in the middle and lower basin of the Yangtze River, China. *Remote Sens. Environ.* **2017**, *190*, 107–121. [CrossRef]
21. Wang, X.; Song, K.; Wen, Z.; Liu, G.; Shang, Y.; Fang, C.; Lyu, L.; Wang, Q. Quantifying Turbidity Variation for Lakes in Daqing of Northeast China Using Landsat Images From 1984 to 2018. *IEEE J. Sel. Top. Appl. Earth Obs. Remote Sens.* **2021**, *14*, 8884–8897. [CrossRef]
22. Feng, L.; Hu, C.; Chen, X.; Tian, L.; Chen, L. Human induced turbidity changes in Poyang Lake between 2000 and 2010: Observations from MODIS. *J. Geophys. Res. Ocean.* **2012**, *117*, C07006. [CrossRef]

23. Antoine, D.; André, J.M.; Morel, A. Oceanic primary production: 2. Estimation at global scale from satellite (coastal zone color scanner) chlorophyll. *Glob. Biogeochem. Cycles* **1996**, *10*, 57–69. [CrossRef]
24. Liu, D.; Duan, H.; Loiselle, S.; Hu, C.; Zhang, G.; Li, J.; Yang, H.; Thompson, J.R.; Cao, Z.; Shen, M.; et al. Observations of water transparency in China's lakes from space. *Int. J. Appl. Earth Obs. Geoinf.* **2020**, *92*, 102187. [CrossRef]
25. Nechad, B.; Ruddick, K.G.; Park, Y. Calibration and validation of a generic multisensor algorithm for mapping of total suspended matter in turbid waters. *Remote Sens. Environ.* **2010**, *114*, 854–866. [CrossRef]
26. Rodríguez-López, L.; Duran-Llacer, I.; González-Rodríguez, L.; Cardenas, R.; Urrutia, R. Retrieving water turbidity in araucanian lakes (South-central chile) based on multispectral landsat imagery. *Remote Sens.* **2021**, *13*, 3133. [CrossRef]
27. Mouw, C.B.; Greb, S.; Aurin, D.; DiGiacomo, P.M.; Lee, Z.; Twardowski, M.; Binding, C.; Hu, C.; Ma, R.; Moore, T.; et al. Aquatic color radiometry remote sensing of coastal and inland waters: Challenges and recommendations for future satellite missions. *Remote Sens. Environ.* **2015**, *160*, 15–30. [CrossRef]
28. Palmer, S.C.; Kutser, T.; Hunter, P.D. Remote sensing of inland waters: Challenges, progress and future directions. *Remote Sens. Environ.* **2015**, *157*, 1–8. [CrossRef]
29. Spyrakos, E.; O'Donnell, R.; Hunter, P.D.; Miller, C.; Scott, M.; Simis, S.G.H.; Neil, C.; Barbosa, C.C.F.; Binding, C.E.; Bradt, S.; et al. Optical types of inland and coastal waters. *Limnol. Oceanogr.* **2018**, *63*, 846–870. [CrossRef]
30. Neil, C.; Spyrakos, E.; Hunter, P.D.; Tyler, A.N. A global approach for chlorophyll-a retrieval across optically complex inland waters based on optical water types. *Remote Sens. Environ.* **2019**, *229*, 159–178. [CrossRef]
31. Song, K.; Wen, Z.; Jacinthe, P.A.; Zhao, Y.; Du, J. Dissolved carbon and CDOM in lake ice and underlying waters along a salinity gradient in shallow lakes of Northeast China. *J. Hydrol.* **2019**, *571*, 545–558. [CrossRef]
32. Song, K.; Wang, Q.; Liu, G.; Jacinthe, P.-A.; Li, S.; Tao, H.; Du, Y.; Wen, Z.; Guo, W.; Wang, Z.; et al. A unified model for high resolution mapping of global lake (>1 ha) clarity using Landsat imagery data. *Sci. Total Environ.* **2022**, *810*, 151188. [CrossRef]
33. Li, S.; Chen, F.; Song, K.; Liu, G.; Tao, H.; Xu, S.; Wang, X.; Mu, G. Mapping the trophic state index of eastern lakes in China using an empirical model and Sentinel-2 imagery data. *J. Hydrol.* **2022**, *608*, 127613. [CrossRef]
34. Wang, S.M.; Dou, H.S. *Lakes in China*; Science press: Beijing, China, 1998.
35. APHA. *Standard Methods for the Examination of Water and Wastewater*, 20th ed.; American Public Health Association: Washington, DC, USA; American Water Works Association: Austin, TX, USA; Water Environment Federation: Alexandria, VA, USA, 1998.
36. Bricaud, A.; Babin, M.; Morel, A.; Claustre, H. Variability in the chlorophyll-specific absorption coefficients of natural phytoplankton: Analysis and parameterization. *J. Geophys. Res. Ocean.* **1995**, *100*, 13321–13332. [CrossRef]
37. Warren, M.A.; Simis, S.G.; Selmes, N. Complementary water quality observations from high and medium resolution Sentinel sensors by aligning chlorophyll-a and turbidity algorithms. *Remote Sens. Environ.* **2021**, *265*, 112651. [CrossRef]
38. Sass, G.Z.; Creed, I.F.; Bayley, S.E.; Devito, K.J. Understanding variation in trophic status of lakes on the Boreal Plain: A 20 year retrospective using Landsat TM imagery. *Remote Sens. Environ.* **2007**, *109*, 127–141. [CrossRef]
39. Wickel, B.A.; Lehner, B.; Sindorf, N. HydroSHEDS: A Global Comprehensive Hydrographic Dataset. In Proceedings of the AGU Fall Meeting Abstracts, San Francisco, CA, USA, 10–14 September 2007; American Geophysical Union: Washington, DC, USA, 2007; Volume 2007, p. H11H–05.
40. Messager, M.L.; Lehner, B.; Grill, G.; Nedeva, I.; Schmitt, O. Estimating the volume and age of water stored in global lakes using a geo-statistical approach. *Nat. Commun.* **2016**, *7*, 1–11. [CrossRef]
41. Ruddick, K.; Vanhellemont, Q.; Yan, J.; Neukermans, G.; Wei, G.; Shang, S. Variability of suspended particulate matter in the Bohai Sea from the geostationary Ocean Color Imager (GOCI). *Ocean. Sci. J.* **2012**, *47*, 331–345. [CrossRef]
42. Ouma, Y.O.; Noor, K.; Herbert, K. Modelling reservoir chlorophyll-a, TSS, and turbidity using Sentinel-2A MSI and Landsat-8 OLI satellite sensors with empirical multivariate regression. *J. Sens.* **2020**, *2020*, 1–21. [CrossRef]
43. Feng, L.; Hou, X.; Zheng, Y. Monitoring and understanding the water transparency changes of fifty large lakes on the Yangtze Plain based on long-term MODIS observations. *Remote Sens. Environ.* **2019**, *221*, 675–686. [CrossRef]
44. Moore, T.S.; Dowell, M.D.; Bradt, S.; Verdu, A.R. An optical water type framework for selecting and blending retrievals from bio-optical algorithms in lakes and coastal waters. *Remote Sens. Environ.* **2014**, *143*, 97–111. [CrossRef]
45. Page, B.P.; Olmanson, L.G.; Mishra, D.R. A harmonized image processing workflow using Sentinel-2/MSI and Landsat-8/OLI for mapping water clarity in optically variable lake systems. *Remote Sens. Environ.* **2019**, *231*, 111284. [CrossRef]
46. Matsushita, B.; Yang, W.; Yu, G.; Oyama, Y.; Yoshimura, K.; Fukushima, T. A hybrid algorithm for estimating the chlorophyll-a concentration across different trophic states in Asian inland waters. *ISPRS J. Photogramm. Remote Sens.* **2015**, *102*, 28–37. [CrossRef]
47. Smith, M.E.; Lain, L.R.; Bernard, S. An optimized chlorophyll a switching algorithm for MERIS and OLCI in phytoplankton-dominated waters. *Remote Sens. Environ.* **2018**, *215*, 217–227. [CrossRef]
48. Babin, M.; Stramski, D.; Ferrari, G.M.; Claustre, H.; Bricaud, A.; Obolensky, G.; Hoepffner, N. Variations in the light absorption coefficients of phytoplankton, nonalgal particles, and dissolved organic matter in coastal waters around Europe. *J. Geophys. Res. Ocean.* **2003**, *108*, 3211. [CrossRef]
49. Song, K.; Liu, G.; Wang, Q.; Wen, Z.; Lyu, L.; Du, Y.; Sha, L.; Fang, C. Quantification of lake clarity in China using Landsat OLI imagery data. *Remote Sens. Environ.* **2020**, *243*, 111800. [CrossRef]
50. IOCCG. *Earth Observations in Support of Global Water Quality Monitoring*; IOCCG Report; Greb, S., Dekker, A., Binding, C., Eds.; International Ocean Colour Coordinating Group (IOCCG): Dartmouth, NS, Canada, 2018.

51. Kutser, T.; Verpoorter, C.; Paavel, B.; Tranvik, L.J. Estimating lake carbon fractions from remote sensing data. *Remote Sens. Environ.* **2015**, *157*, 138–146. [CrossRef]
52. Mi, H.; Fagherazzi, S.; Qiao, G.; Hong, Y.; Fichot, C.G. Climate change leads to a doubling of turbidity in a rapidly expanding Tibetan lake. *Sci. Total Environ.* **2019**, *688*, 952–959. [CrossRef]
53. Wang, C.; Wei, Z.; Zhao, Y.; Bai, L.; Jiang, H.; Xu, H.; Xu, Y. Resuspension and settlement characteristics of lake sediments amended by phosphorus inactivating materials: Implications for environmental remediation. *J. Environ. Manag.* **2022**, *302*, 113892. [CrossRef]
54. Kiselev, V.; Bulgarelli, B.; Heege, T. Sensor independent adjacency correction algorithm for coastal and inland water systems. *Remote Sens. Environ.* **2015**, *157*, 85–95. [CrossRef]
55. Ma, R.; Duan, H.; Liu, Q.; Loiselle, S.A. Approximate bottom contribution to remote sensing reflectance in Taihu Lake, China. *J. Great Lakes Res.* **2011**, *37*, 18–25. [CrossRef]
56. Cleveland, J.; Weidemann, A. Quantifying absorption by aquatic particles: A multiple scattering correction for glass-fiber filters. *Limnol. Oceanogr.* **2013**, *38*, 1321–1327. [CrossRef]
57. Wang, X.; Siegert, F.; Zhou, A.; Franke, J. Glacier and glacial lake changes and their relationship in the context of climate change, Central Tibetan Plateau 1972–2010. *Global Planet Chang.* **2013**, *111*, 246–257. [CrossRef]
58. Jeffrey, S.W.; Humphrey, G.F. New Spectrophotometric Equations for Determing Chlorophyll a, b, c1 and c2 in Higher Plants, Algae and Natural Phycoplankton. *J. Plant Physiol.* **1975**, *167*, 191–194.
59. Babin, M.; Stramski, D.; Ferrari, G. Variations in the light absorption coefficients of phytoplankton, nonalgal particles, and dissolved organic mat-ter in coastal waters around Europe. *J. Geophys Res. Oceans* **2003**, *108*.

Disclaimer/Publisher's Note: The statements, opinions and data contained in all publications are solely those of the individual author(s) and contributor(s) and not of MDPI and/or the editor(s). MDPI and/or the editor(s) disclaim responsibility for any injury to people or property resulting from any ideas, methods, instructions or products referred to in the content.